

Thermally Activated Delayed Fluorescent Dendrimers for High-efficiency Solution-Processed Organic Light Emitting Diodes

Dianming Sun¹, Anna Köhler², Eli Zysman-Colman¹

eli.zysman-colman@st-andrews.ac.uk

¹Organic Semiconductor Centre, EaStCHEM School of Chemistry, University of St Andrews, St Andrews KY16 9ST, UK.

²Soft Matter Optoelectronics, BIMF & BPI, University of Bayreuth, Universitätsstraße 30, 95447 Bayreuth, Germany.

Keywords: TADF dendrimers, host-free OLEDs, solution-processing, external quantum efficiency, carbazole.

ABSTRACT

A series of TADF dendrimers have been developed to resolve the conflicting requirements of achieving simultaneously a small ΔE_{ST} and a large oscillator strength by adopting a dendron that combines both a meta- and para- connected dendritic donor. The role of meta- and para- linkage has been revealed.

1 Introduction

Organic thermally activated delayed fluorescence (TADF) materials¹⁻⁸ have evolved rapidly since the first report of high-efficiency organic light-emitting diodes (OLEDs) showing greater than 20% maximum external quantum efficiency (EQE_{max}).⁹ A number of benchmark red,¹⁰⁻¹³ green,¹⁴ and blue¹⁵ emitters have already been reported where the OLEDs show greater than 20% EQE_{max}, representing the significant recent successes and promise that TADF materials play for next-generation OLEDs. However, the excellent performance of these devices relies on vacuum-deposition fabrication, which is costly and materials-wasteful. Fabrication of OLEDs using solution-processing techniques is generally considered as a solution to realize low-cost, large-area OLED displays and solid-state luminaires.¹⁶ Solution-processed OLED fabrication techniques such as spin-coating^{17, 18} and ink-jet printing¹⁹ are advantageous as the device architecture is simpler, less material is lost during film formation and large-area display fabrication using these mature technologies becomes much more scalable. What is required are devices that exhibit comparable performance metrics to vacuum-deposited devices, and this is underpinned by high-performance solution-processable emitter materials.

Unlike small molecules, dendrimers and polymers allow for facile solution-processed manufacture of large-area devices due to their superior film-forming ability, excellent thermal and morphological stability, and high affinity for substrates.²⁰⁻²³ The molecular weight distribution of polymers, however, normally leads to batch-to-batch deviation of their (photo)physical properties. Unlike polymers, dendrimers have a well-defined molecular weight. Moreover, in general, most TADF dendrimers do not need to be dispersed into host matrices to suppress concentration or aggregation-caused quenching of the emission and/or exciton annihilation. Thus, high-efficiency

non-doped OLEDs can be fabricated, leading to a simplified device architecture.

To date, there have been only a handful of reports using TADF dendrimers,²⁴⁻³⁹ most of which disclose devices that possess efficiencies that are far from the state-of-the-art of small molecule TADF OLEDs. Slow progress due to a paucity of examples of TADF dendrimers and a poor understanding of their photophysics have hampered the development of dendrimer TADF OLEDs. In general, the relative position of donors and acceptors has a significant effect on the TADF properties.⁴⁰ Different substitution modes alter the spatial overlap of the hole density and electron density distributions of the HOMO and LUMO, respectively. This leads to different ΔE_{ST} values, thus affecting the efficiency and nature of the RISC process of the TADF materials. This analysis has motivated us to compare a *para*-bridged dendrimer with its *meta*-based analogues to assess the influence of the *para*- versus *meta*-linked dendrons. As a result, a dendrimer combining the advantages of both *para*- and *meta*-dendrimers has been developed for high-performance solution-processed OLEDs.

2 Experiment

All neat film samples were prepared by spin-coating 10 mg/mL chloroform solutions of dendrimers. The time-resolved emission measurements were obtained using an iCCD camera by exponentially increasing delay and gating times where the gating time is kept lower by 10 times compared to the delay time. All measurements were recorded under vacuum unless otherwise stated. The OLED devices were fabricated using a bottom-emitting architecture. A pre-patterned indium tin oxide (ITO) glass substrate was used as the anode. PEDOT:PSS8000 was spin-coated onto the clean ITO substrate as a hole-injection layer, then the 10 mg/mL dendrimers in chlorobenzene solution were spin-coated to form the emissive layer (EML). TmPyPB, LiF and Al were each subsequently vacuum-deposited onto the EML.

3 Results and Discussion

3.1 Design strategy

To assess the effect of the substitution position of the donor dendrons on the dendrimer emitters, a *meta*-

dendrimer and a dendrimer with mixed *para*- and *meta*-connected dendrons were designed and their photophysical properties and OLED device performance compared with the *para*-analogue (Fig. 1).

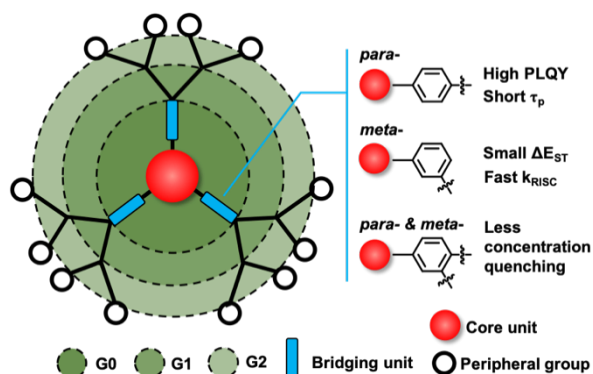


Fig. 1 Schematic diagram of dendrimer structures that linked through *para*-or/*meta*-connections.

3.2 Morphologies and thermal stabilities

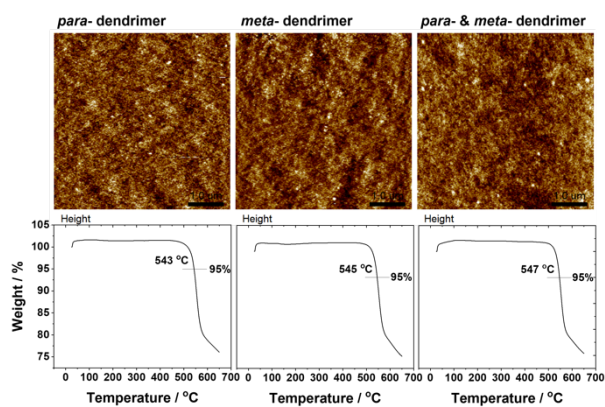


Fig. 2 (Top) AFM topographical images of the solution-processed neat films of *para*-, *meta*- and *para-meta*-dendrimers. (Bottom) Thermogravimetric analysis (TGA) performed under a nitrogen atmosphere at a heating rate of $10\text{ }^{\circ}\text{C min}^{-1}$.

The film-forming ability of these dendrimers were investigated by atomic force microscopy (AFM). As shown in Fig. 2, the AFM images display fairly smooth and homogeneous morphologies. The AFM images show that the films are free of particle aggregation or pin holes, suggesting good film forming ability of the dendrimers. The thermal stability has been assessed by thermogravimetric analysis (TGA). All dendrimers have remarkably high decomposition (T_d) temperature of between 543 to 547° .

3.3 Time-resolved PL

The neat film photophysics of the three dendrimers at 300 K and at 5 K are shown in Fig. 3a-c). The prompt emission at both 300 K and 5 K in neat films is broad and unstructured, which implies an excited state with strong

charge transfer (CT) character. The prompt emission of the *para*-dendrimer still closely resembles that of *meta*-dendrimer. The energy levels of the lowest singlet CT states determined from the onsets of the corresponding prompt fluorescence spectra at 5 K are 2.78 , 2.81 and 2.63 eV for *para*-, *meta*- and *para-meta*-dendrimer, respectively. The spectra obtained at 5 K after a time delay of 30 ms are ascribed to phosphorescence. The phosphorescence spectrum for the *para*-dendrimer is structured with a major peak at 486 nm (2.55 eV) and a low energy feature around 510 nm (2.43 eV) that we ascribe to poorly resolved vibrational transitions. The energies of the T_1 state of *para*-dendrimer and *meta*-dendrimer were determined to be 2.69 and 2.72 eV , respectively, leading to the same ΔE_{ST} value of 90 meV . The similarities in their S_1 and T_1 states indicate that the presence of *para*- or *meta*-connections between donor and acceptor groups has only a small effect on the nature of the excited states. The energy of the T_1 state of the *para-meta*-dendrimer is located at 2.59 eV , leading to the smallest ΔE_{ST} value of 40 meV of the three materials.

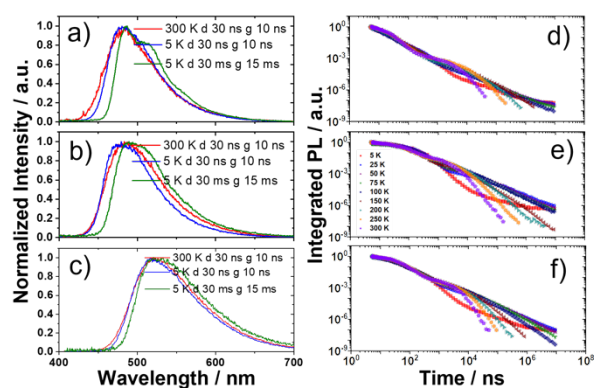


Fig. 3 Prompt fluorescence (d: 30 ns/g : 10 ns) at 300 K (red solid line) and at 5 K (blue solid line), Phosphorescence with detection in the ms range (d: 30 ms/g : 15 ms) at 5 K (green solid line) of *para*- (a&d), *meta*- (b&e) and *para-meta*-dendrimer (c&f) neat films. In the legend, d refers to delay time and g refers to gate width. Temperature-dependent time-resolved PL decay of neat films. The decays were obtained by integrating each time-resolved spectrum across the full spectral range. ($\lambda_{\text{exc}}=355\text{ nm}$).

Fig. 3d-f shows the PL decay curves of the neat films. All decays at 300 K show two regimes: a prompt fluorescence (PF) regime followed by a delayed fluorescence (DF) component from about 500 ns onwards. The intensity of the DF decreases upon cooling and vanishes at 5 K yet, for the *meta*- and *para-meta*-dendrimers, most thermal activation occurs between 5 and 25 K , implying a very efficient RISC. Based on this thermal activation, the relevant singlet-triplet gaps for *meta*- and *para-meta*-dendrimers are likely to be smaller

than predicted by the steady-state optical data at 5K.

3.4 OLEDs

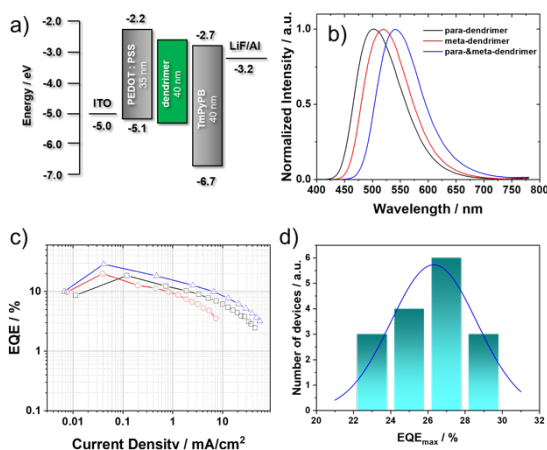


Fig. 4 Electroluminescence characteristics of host-free OLEDs using *para*-, *meta*- and *para-meta*-dendrimers as emitters. (a) Device configuration. (b) Normalized electroluminescence spectra. (c) EQE versus current density. (e) Statistical histogram of EQE_{max} for *para*-&*meta*-dendrimer based OLEDs.

We next fabricated simple bilayer devices consisting of: ITO/PEDOT:PSS (35 nm)/dendrimer (40 nm)/ TmPyPB (40 nm)/LiF (1 nm)/ Al (100 nm). The emissive layer is composed of a neat film of one of the dendrimers. The schematic diagram of the device structure together with energy levels of each layer are shown in **Fig. 4a**. The electroluminescence spectra (EL) of these devices are presented in **Fig. 4b**. The gradual red-shift of the EL spectra is consistent with the trends observed for the PL spectra in neat films. **Fig. 4c** shows the EQE versus current density for these devices. The EQE_{max} of the best performing examples of devices are 18.5%, 19.9% and 28.7%, respectively. It is clear that the performance of the *para-meta*-dendrimer based device is significantly improved compared to the those of the other two OLEDs. Notably, according to the histogram of EQE_{max} values (Fig. 4d), the average EQE_{max} of 26.3% for *para-meta*-dendrimer OLED is close to the highest obtained EQE_{max} (28.7%), indicating high batch-to-batch reproducibility.

The device performance was further optimized to reduce the efficiency roll-off observed in the non-doped OLEDs by blending 30 wt% of OXD-7 into the emitting layer. As shown in **Fig. 5**, the optimized device with the OXD-7 shows the same low turn on voltage at 3.1 V and the EL spectrum also remains the same. The performance of the optimized device is close to that of original device as indicated by the similar EQE_{max} of 28.4%. Importantly, a significant improvement in efficiency roll-off can be observed for the optimized device where the EQE reached 22.7% at a luminance of 500 $cd\ m^{-2}$ (**Fig. 5d**).

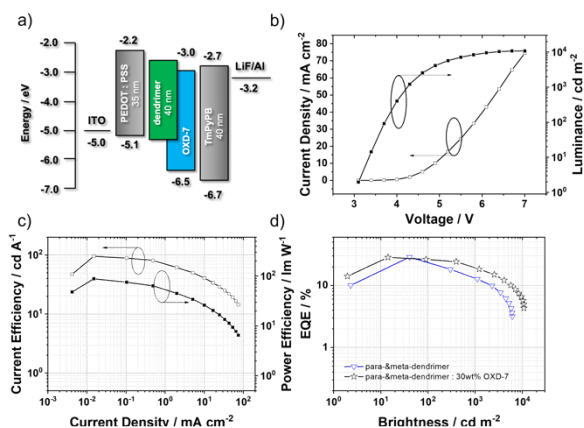


Fig. 5 Optimized electroluminescence characteristics of host-free OLEDs based on *para-meta*-dendrimer: 30 wt% OXD-7 emitting layer. (a) Device configuration. (b) Current density and luminance versus driving voltage characteristics. (c) Current efficiency and power efficiency versus current density. (d) EQE versus brightness (Comparison with the device without doping OXD-7 in the emitting layer).

4 Conclusions

By taking advantage of the molecular design features embedded within *para-meta*-dendrimer we have rationalized the remarkable improvement in the photophysical properties and device performance through the synergistic effects of *meta*- and *para*-connected donor dendrons to the central acceptor core. We believe that the dendrimer design strategy disclosed in our study provides a route to high-performance solution-processed TADF OLEDs and evidences the full potential of dendrimers as emissive materials.

References

1. Y. Tao, K. Yuan, T. Chen, P. Xu, H. Li, R. Chen, C. Zheng, L. Zhang and W. Huang, *Adv. Mater.* **26** (47), 7931-7958 (2014).
2. Y. Im, M. Kim, Y. J. Cho, J.-A. Seo, K. S. Yook and J. Y. Lee, *Chem. Mater.* **29**, 1946-1963 (2017).
3. M. Y. Wong and E. Zysman-Colman, *Adv. Mater.* **29** (22), 1605444 (2017).
4. Z. Yang, Z. Mao, Z. Xie, Y. Zhang, S. Liu, J. Zhao, J. Xu, Z. Chi and M. P. Aldred, *Chem. Soc. Rev.* **46** (3), 915-1016 (2017).
5. X. Cai and S. J. Su, *Adv. Funct. Mater.* **28**, 1802558 (2018).
6. Y. Liu, C. Li, Z. Ren, S. Yan and M. R. Bryce, *Nat. Rev. Mater.* **3**, 18020 (2018).
7. Y. Zou, S. Gong, G. Xie and C. Yang, *Adv. Opt. Mater.* **6** (23), 1800568 (2018).
8. X. Liang, Z.-L. Tu and Y.-X. Zheng, *Chem. Eur. J.* **25** (22), 5623-5642 (2019).
9. H. Uoyama, K. Goushi, K. Shizu, H. Nomura and C. Adachi, *Nature* **492** (7428), 234-238 (2012).
10. W. Zeng, H. Y. Lai, W. K. Lee, M. Jiao, Y. J. Shiu, C. Zhong, S. Gong, T. Zhou, G. Xie, M. Sarma, K. T. Wong, C. C. Wu and C. Yang, *Adv. Mater.* **30** (5), 1704961 (2017).

11. Y. Yuan, Y. Hu, Y.-X. Zhang, J.-D. Lin, Y.-K. Wang, Z.-Q. Jiang, L.-S. Liao and S.-T. Lee, *Adv. Funct. Mater.* **27** (26), 1700986 (2017).
12. J.-X. Chen, K. Wang, C.-J. Zheng, M. Zhang, Y.-Z. Shi, S.-L. Tao, H. Lin, W. Liu, W.-W. Tao, X.-M. Ou and X.-H. Zhang, *Adv. Sci.* **5** (9), 1800436 (2018).
13. J.-X. Chen, W.-W. Tao, W.-C. Chen, Y.-F. Xiao, K. Wang, C. Cao, J. Yu, S. Li, F.-X. Geng, C. Adachi, C.-S. Lee and X.-H. Zhang, *Angew. Chem. Int. Ed.* **58** (41), 14660-14665 (2019).
14. T.-L. Wu, M.-J. Huang, C.-C. Lin, P.-Y. Huang, T.-Y. Chou, R.-W. Chen-Cheng, H.-W. Lin, R.-S. Liu and C.-H. Cheng, *Nat. Photon.* **12** (4), 235-240 (2018).
15. D. H. Ahn, S. W. Kim, H. Lee, I. J. Ko, D. Karthik, J. Y. Lee and J. H. Kwon, *Nat. Photon.* **13** (8), 540-546 (2019).
16. Y. Xie and Z. Li, *J. Polym. Sci. A Polym. Chem.* **55** (4), 575-584 (2017).
17. Y. Yuan, G. Giri, A. L. Ayzner, A. P. Zoombelt, S. C. Mannsfeld, J. Chen, D. Nordlund, M. F. Toney, J. Huang and Z. Bao, *Nat. Commun.* **5**, 3005 (2014).
18. D. B. Mitzi, L. L. Kosbar, C. E. Murray, M. Copel and A. Afzali, *Nature* **428** (6980), 299-303 (2004).
19. J. Heinzl and C. Hertz, in *Advances in electronics and electron physics* (Elsevier, 1985), Vol. 65, pp. 91-171.
20. C. R. McNeill and N. C. Greenham, *Adv. Mater.* **21** (38-39), 3840-3850 (2009).
21. J. L. Brédas and R. R. Chance, *Conjugated polymeric materials: opportunities in electronics, optoelectronics, and molecular electronics*. (Springer Science & Business Media, 2012).
22. S.-C. Lo and P. L. Burn, *Chem. Rev.* **107** (4), 1097-1116 (2007).
23. P. L. Burn, S. C. Lo and I. D. Samuel, *Adv. Mater.* **19** (13), 1675-1688 (2007).
24. K. Albrecht, K. Matsuoka, K. Fujita and K. Yamamoto, *Angew. Chem. Int. Ed.* **54** (19), 5677-5682 (2015).
25. X. Ban, W. Jiang, T. Lu, X. Jing, Q. Tang, S. Huang, K. Sun, B. Huang, B. Lin and Y. Sun, *J. Mater. Chem. C* **4** (37), 8810-8816 (2016).
26. Y. Li, G. Xie, S. Gong, K. Wu and C. Yang, *Chem. Sci.* **7** (8), 5441-5447 (2016).
27. J. Luo, S. Gong, Y. Gu, T. Chen, Y. Li, C. Zhong, G. Xie and C. Yang, *J. Mater. Chem. C* **4** (13), 2442-2446 (2016).
28. K. Albrecht, K. Matsuoka, D. Yokoyama, Y. Sakai, A. Nakayama, K. Fujita and K. Yamamoto, *Chem. Comm.* **53** (16), 2439-2442 (2017).
29. X. Ban, W. Jiang, K. Sun, B. Lin and Y. Sun, *ACS Appl. Mater. Interfaces* **9** (8), 7339-7346 (2017).
30. J. Li, X. Liao, H. Xu, L. Li, J. Zhang, H. Wang and B. Xu, *Dyes Pigm.* **140**, 79-86 (2017).
31. Y. Li, T. Chen, M. Huang, Y. Gu, S. Gong, G. Xie and C. Yang, *J. Mater. Chem. C* **5** (14), 3480-3487 (2017).
32. K. Matsuoka, K. Albrecht, K. Yamamoto and K. Fujita, *Sci. Rep.* **7** (1), 1-9 (2017).
33. K. Sun, D. Chu, Y. Cui, W. Tian, Y. Sun and W. Jiang, *Org. Electron.* **48**, 389-396 (2017).
34. K. Sun, Y. Sun, T. Huang, J. Luo, W. Jiang and Y. Sun, *Org. Electron.* **42**, 123-130 (2017).
35. K. Albrecht, K. Matsuoka, K. Fujita and K. Yamamoto, *Mater. Chem. Front.* **2** (6), 1097-1103 (2018).
36. M. Godumala, S. Choi, H. J. Kim, C. Lee, S. Park, J. S. Moon, K. Si Woo, J. H. Kwon, M. J. Cho and D. H. Choi, *J. Mater. Chem. C* **6** (5), 1160-1170 (2018).
37. K. Matsuoka, K. Albrecht, A. Nakayama, K. Yamamoto and K. Fujita, *ACS Appl. Mater. Interfaces* **10** (39), 33343-33352 (2018).
38. D. Liu, W. Tian, Y. Feng, X. Zhang, X. Ban, W. Jiang and Y. Sun, *ACS Appl. Mater. Interfaces* **11** (18), 16737-16748 (2019).
39. X. Wang, S. Wang, J. Lv, S. Shao, L. Wang, X. Jing and F. Wang, *Chem. Sci.* **10** (10), 2915-2923 (2019).
40. F.-M. Xie, J.-X. Zhou, Y.-Q. Li and J.-X. Tang, *J. Mater. Chem. C* **8**, 9476-9494 (2020).